Hindawi
Shock and Vibration
Volume 2018, Article ID 7036726, 14 pages
https://doi.org/10.1155/2018/7036726

*Research Article*

# Theoretical Calculation and Experimental Analysis on Initial Shock Pressure of Borehole Wall under Axial Decoupled Charge

**Xiaoming Lou**,[1,2] **Zhenchang Wang**,[1,2] **Bigang Chen**,[1,2] **and Jin Yu**[3]

[1]*College of Zijin Mining, Fuzhou University, Fuzhou 350116, China*
[2]*Institute of Blasting Technology, Fuzhou University, Fuzhou 350116, China*
[3]*Institute of Geotechnical Engineering, Huaqiao University, Xiamen 361021, China*

Correspondence should be addressed to Xiaoming Lou; 331261323@qq.com

Received 23 October 2017; Revised 6 March 2018; Accepted 12 June 2018; Published 4 July 2018

Academic Editor: Longjun Dong



This paper attempts to calculate the exact initial shock pressure of borehole wall induced by the blasting with axially decoupled charge. For this purpose, Starfield superposition was introduced considering the attenuation and superposition of blasting pressure, and the theoretical solution of initial borehole wall pressure was obtained for the upper and middle air-decked charging structures. Then, the explosive pressure field around the borehole was measured by cement mortar models and a dynamic pressure test system, and the pressures at multiple measuring points were simulated with numerical models established by ANSYS/LS-DYNA. The results show that the deviations between simulated and theoretical pressures are smaller than 10%, indicating the reliability of the theoretical formula derived by Starfield superposition. For the upper air-decked charging structure, the initial shock pressure of the charging section followed a convex distribution, with the peak value near the charge centre. With the increase in the distance from the charging section, the borehole wall shock pressure in the air gap underwent a sharp decline initially before reaching a relatively constant level. The minimum pressure was observed at the hole collar. For the middle air-decked charging structure, the pressures at both ends of the charging section obeyed a convex distribution, with the peak value near the charge centre. Finally, the author optimized air-decked charging structure of periphery boreholes within Grade III surrounding rocks of Banjie tunnel, China, and proved the enhancement effect of the theoretical findings on smooth blasting. The research findings provide valuable references to the theoretical and experimental calculation of air column length and other key parameters of air-deck blasting and shed new light on the charging structure determination of smooth blasting and blasting vibration control for the excavation of large-section, deep mining roadways.

## 1. Research Status

During the excavation of deep roadway or tunnel under high crustal pressure, the stability of the surrounding rock is dependent on the effect of smooth blasting, which itself hinges on the selection of axial decoupling coefficient. Concerning the close ties between the coefficient, the air gap, and the initial shock pressure of the borehole wall, below is a brief review of the existing studies on mine blasting, especially air-deck blasting, that involves these three elements.

In previous research, the initial shock pressure of borehole wall with air-decked charge is considered as 8~11 times the quasi-static pressure of the detonation gas [1], provided that the borehole wall is rigid and subject to orthogonal impact from the detonation wave and that the shock waves which attenuate and superpose along the borehole axis are negligible; i.e., the initial shock pressure of borehole wall is uniformly distributed in the axial direction. This conclusion may apply to short air gap or axially coupled charge but does not suit long air gap or axially decoupled charge. Hence, it is necessary to explore the initial shock pressure of borehole wall under axially decoupled charge.

To disclose the mechanism of air-deck blasting, Kabwe [2] suggested that the surrounding rock can be enhanced by repeated oscillation of shock wave at air space sections and verified the suggestion with the distribution of rock fragments after blasting with top air-decked charge (hereinafter referred to as "top air-deck blasting") at Chimiwungo Pit of

Lumwana, an open-pit copper mine. Similarly, Jhanwar and Jethwa [3], through an air-deck blasting at an open-pit coal mine in India, discovered that the blasting method can reduce the yield of fines and boulders, and that the length of air space directly bears on the distribution of rock fragments. Fourney et al. [4] concluded that, in top air-deck blasting, the shock wave is reflected upon reaching the plug, and the shock pressure on the surrounding rock lasts 2~5 times that under coupled charge. Moreover, it is critical to determine a proper length of air gap, because the surrounding rock will not be further broken if the pressure of the reflected shock wave fails to surpass the tensile strength of the rock.

Yang et al. [5] numerically simulated the distribution of initial shock pressure at different air gap ratios, pointing out that the optimal directional fracture effect appears at the air gap ratio of 33.3%~50% in slit-charge blasting. Saharan et al. [6] proposed to improve the energy utilization rate of explosives through rational setting of air gap and plug lengths and achieved the expected improvement with different combinations of air gap and plug. Furthermore, Park and Jeon [7] put forward an air-deck blasting method with a thin paper-tube and quantified its shock absorption effect and tunnelling efficiency through numerical simulation and experiments. Roy et al. [8] applied the mature air-deck blasting technique of open-pit mining and tunnelling to an underground coal mine in India and succeeded in enhancing the blasting effect and controlling the deflagration and harmful gases.

Over the years, much research has been done on the pressure distribution of borehole wall. Despite the lack of direct measuring methods, the borehole wall pressure has been estimated with various empirical formulas or detonation theories [9]. Taking borehole wall pressure as the basis of blasting design, Cunningham [10] derived borehole wall pressure via polynomial decay and presented an alternative to the pressure. Otuonye et al. [11] calculated borehole wall pressure through lab tests on stemming movement. Homment et al. [12] determined borehole wall pressure based on the expanding volume of blasting cavity. Swoboba [13] developed a novel numerical model on the propagation of explosion pressure, which describes the crack propagation in the borehole wall and deduces borehole wall pressure based on blasting cavity or crack volume. Likewise, Liu and Katsabanis [14] created a new computing method after exploring the initial shock pressure of borehole wall. Yilmaz and Unlu [15] provided the estimation formula of borehole wall pressure in light of the explosion pressure expressions under decoupled charge in [16, 17].

With the development of computer technology and intelligent testing, a series of new approaches have been introduced to reveal the dynamic effect of rock blasting, e.g., numerical simulation and model test. With the aid of LS-DYNA and FLAC3D, Jiang et al. [18] investigated the blasting damage of vertical crater retreat (VCR) mining method, laying the theoretical basis for rational control of stope boundaries and optimization of blasting parameters. Through numerical simulation of bottom air-deck blasting, Wu et al. [19] studied the dynamic pressure features and failure mechanism of near-field boreholes, compared the dynamic pressure features of different detonation methods, and found that indirect initiation can easily destroy the bottom rock of borehole by enhancing static function intensity.

Focusing on directional pressure-relief blasting, Xiao et al. [20] carried out cement mortar model tests on the dynamic strain of borehole wall and other parts. The test results are in good agreement with those of numerical simulation, indicating that the pressure-relief effect of the borehole can protect the wall materials and the bottom air gap columns. Ma et al. [21] tested 4 types of millisecond blasting models with three-circle boreholes, aiming to find the blast damage on the surrounding rock in vertical shaft excavation and put forward effective damage control measures. Zhao et al. [22] performed a blasting model test with similar materials and dosages by Froude scaling and provided theoretical and empirical references to the selection of materials and charging conditions for blasting test models.

The above studies open a new direction for quantifying the distribution of initial shock pressure in borehole wall. Considering air-deck blasting, Yang et al. [23] probed into the borehole pressure distribution under different charging conditions and disclosed the heterogeneous pressure distribution across borehole wall: the initial shock pressure peaks at the centre of the charging section, far higher than that in the air gap. This means the initial shock pressure of borehole wall distributes unevenly along the axial direction. Nevertheless, there is no report on the mathematical expressions of the uneven distribution pattern.

Under coupled/decoupled charge, Ling [24] tested the initial shock pressure of cement mortar and organic glass and obtained the initial shock pressure at each point of borehole wall. Using manganese-copper piezoresistor, Ni et al. [25] measured the peak initial shock pressure produced by ammonium nitrate explosive, emulsion explosive, and water-gel explosive in granite and concrete and conducted a regression analysis of the relationship between borehole wall pressure and the incident angle. Their research shows the correlation between the initial shock pressure and the distance to the explosive source along the borehole axis. Nonetheless, the finding is only suitable for single-stage charging. Further research is needed to ascertain the distribution of borehole wall pressure of double- or multistage charging.

## 2. Introduction

This paper aims to select a proper axial decoupling coefficient for air-deck blasting. To this end, it is necessary to investigate the air gap and the initial shock pressure of the borehole wall under axial decoupled charge. Here, the Grade III surrounding rock of Banjie tunnel, a 4,806m-long deep-buried tunnel, is taken as the object. The tunnel is one of the three main tunnels in Yongren-Guangdong section of Chengdu-Kunming railway. In the tunnel, the surrounding rock masses are mostly Grade III~V sandstone and sandy mudstone. The tunnel segments through Grades III, IV, and V rocks are, respectively, 4,115m, 530m, and 161m in length. Thus, the object tunnel segment accounts for 85.6%

Table 1: Physical-mechanical parameters of Grade III surrounding rock.

| Density(kg/m$^3$) | Compressive strength(MPa) | Tensile strength (MPa) | Shear strength (MPa) | Longitudinal wave velocity (m/s) | Poisson ratio |
|---|---|---|---|---|---|
| 2700 | 75 | 5.6 | 23.3 | 3350 | 0.23 |

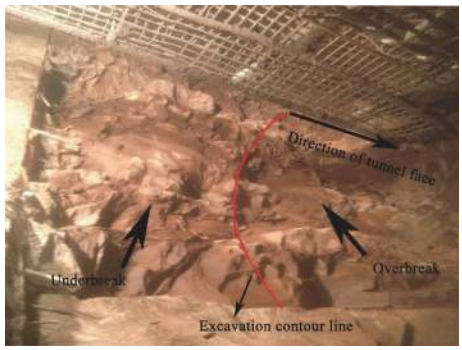


Figure 1: A typical working face with overbreak and underbreak after two-step blasting.

of the total length of Banjie tunnel. The physical-mechanical parameters of Grade III surrounding rock are listed in Table 1.

The previous smooth blasting of Grade III surrounding rock was carried out in two steps with the following parameters: the total sectional area=l16.02 m2, the excavation height= 5.81m (upper stage) and 5.52m (lower stage), and the cyclic advancement=3~3.2m. In the upper stage, the construction parameters are as follows: borehole distance= 50cm (periphery holes) and 80cm (auxiliary holes); and borehole depth=3.8m (periphery holes) and 4m (auxiliary holes). For the five-stage double horizontal wedge cutting, the vertical hole is 4m in depth. The density and detonation velocity of 2# emulsion explosive are 1,300kg/m3 and 3,200m/s, respectively. Due to the high detonator cost and complex process, the periphery holes were charged continuously at the bottom (hereinafter referred to as the continuous bottom charging).

The above blasting structure has some problems that led to an unsuccessful tunnelling. After the smooth blasting on the upper stage, the maximum overbreak was as high as 0.4m near the working face (hole bottom) of the hance, and the maximum underbreak near lining (hole collar) stood at 0.25m. At the vault, the postblast outline exhibited as a large flat plate with severe rockfall. In general, the working face had an uneven contour and barely any visible hole profiles (Figure 1).

The unsuccessful blasting in Banjie tunnelling is mainly caused by inappropriate charging. When continuous charging structure is used at the hole bottom, the over concentrated charging in this section is prone to bring about heavy shock pressure to the borehole wall. The uncharged hole collar, however, tends to result in an underbreak due to insufficient shock pressures.

The unsuccessful blasting is mainly attributable to improper charging. With continuous bottom charging, the charged bottom applied a heavy shock pressure onto borehole wall, while the uncharged hole collar generated so few shock pressure as to cause underbreak. In light of these, Starfield superposition was introduced considering the attenuation and superposition of blasting pressure, and the theoretical solution of the initial borehole wall pressure was obtained for top and middle air-deck blasting.

Meanwhile, the author constructed a stable dynamic pressure test system that avoids the interference and signal distortion of the previous test method and validated the theoretical analysis results through model tests. To determine the optimal axial decoupling coefficient, the distribution features of the initial borehole wall pressure were analysed under different axial decoupling coefficients and contrasted with each other by numerical simulation.

Based on the findings, the peripheral hole charging structure was optimized for the blasting of Grade III rocks in Banjie tunnel, aiming to enhance the smooth blasting effect. Then, the damping effect of air-deck blasting was compared with that of the blasting with continuous bottom charging.

## 3. Theoretical Analysis

*3.1. Starfield Superposition Method.* Starfield superposition treats the column charge as the superposition of a finite number of spherical charges with equal radius, that is, the equal charging principle. Let $d_c$ and $r_e$ be the diameter of column charge and the equivalent radius of spherical charge, respectively. Then, the equal charging principle can be expressed as

$$\frac{4}{3}\pi {r_e}^3 = \pi \left(\frac{d_c}{2}\right)^2 (2r_e) \tag{1}$$

For simplicity, it is assumed that the peak pressure pattern remains the same independent of the detonation order of spherical charges in each unit, such that the peak pressure at a point in the air gap equals the pressure of the shock wave at the point produced by the blasting of the equivalent unit spherical charge lying the closest to the air gap. This value is close to the actual peak pressure and thus satisfies the computing demand [26].

By Starfield superposition, the time effect of the explosion of unit spherical charge cannot be ignored while computing the blasting effect of the column charge. This is because both the detonation velocity of explosives and the longitudinal wave velocity of rock are both in the $10^3$ m/s order of magnitude. Hence, the following exponential function was adopted to depict the time attenuation of the shock wave induced by unit spherical charge [27]:

$$\sigma_r(t) = P_1 e^{-At} \tag{2}$$

where $A$ ($A$=$C_p$(1-2$\mu$)/[$a$(1-$\mu$)$k$]) is the pressure attenuation coefficient of equivalent unit spherical charge $A$=$C_p$(1-2$\mu$)/[$a$(1-$\mu$)$k$] [28, 29]; $C_p$ is the longitudinal wave velocity of rock; $a$ is a constant related to rock properties; and $t$ is the decay time of shock wave.

For a point in the air gap, each equivalent unit spherical charge has a pressure effect on the time of positive pressure. Without the loss of generality, the peak pressure is assumed to occur when the shock wave induced by a unit spherical charge arrived at a specified point. For example, the pressure of a point in the air gap reaches the peak when the shock wave induced by spherical charge unit $k$ propagates to that point, indicating that the pressure induced by the preceding unit $i$ at this point has attenuated. The decay time can be expressed as

$$t = \frac{2r_e(k-i)}{D} + \frac{l_k}{C_p} - \frac{l_i}{C_p} \quad i,k = 1,2\cdots n \tag{3}$$

where $l_i$ is the distance from unit spherical charge $i$ to the specified point in the air gap; $l_k$ is the distance from unit spherical charge $k$ to the specified point in the air gap; $D$ is the detonation velocity of the explosive.

In accordance with the shock wave theory, the peak pressure of shock wave attenuates with the distance, under a single spherical charge, following the pattern below [30]:

$$P_1 = \frac{B}{\overline{R}^{\alpha}} \tag{4}$$

where $\overline{R}$ is a scaled distance; $B$ is a constant; $\alpha$ is the attenuation coefficient of peak shock wave pressure along the borehole axis. The scaled distance is calculated as $\overline{R} = R/\sqrt[3]{Q}$, with $R$ being the distance between the calculation point and the explosive source, and $Q$ being the TNT equivalent of actual charge quantity ($Q$=$Q_sW_s/W_T$, where $Q_s$ is the actual charge quantity; $W_s$ is the specific detonation heat of the explosive; $W_T$ is the specific detonation heat of TNT).

According to (1), the actual charge quantity of a single spherical charge can also be expressed as

$$Q_s = \frac{\sqrt{6}\rho\pi {d_c}^3}{8} \tag{5}$$

Thus, (4) can be rewritten as

$$P_1 = \frac{0.98^{\alpha}\left(\rho W_s/W_T\right)^{\alpha/3} {d_c}^{\alpha} B}{R^{\alpha}} \tag{6}$$

where $\rho$, $W_s$, $B$, and $\alpha$ are constants for specific explosive and surrounding rock.

For better accuracy, the attenuation coefficient of shock pressure along the borehole axis is denoted as $\delta$. Assuming that $K$=0.98$\alpha(\rho W_s/W_T)^{\alpha/3}B$, the peak pressure of a single equivalent unit spherical charge at the specified point can be obtained as

$$P = K\left(\frac{R}{d_c}\right)^{-\delta} e^{-At} \tag{7}$$

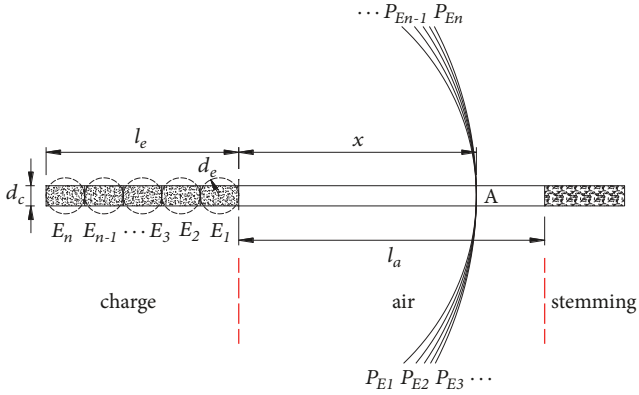


Figure 2: Initial shock pressure of borehole wall with upper air-decked charge.

When ignoring the interaction of explosion for adjacent unit spherical charges, the peak pressure at the specified point of the column charge can be approximately considered as the superposition of the peak stress at the point of all spherical charges.

*3.2. Initial Shock Pressure of Borehole Wall with Upper Air-Decked Charge.* In the upper air-decked charging structure, the length of the air gap is assumed as $l_a$, the charge length at hole bottom as $l_e$, and the charge diameter is $d_c$. As shown in Figure 2, a random point A in the air gap is $x$ ($x \le l_a$) away from the top of the charging section. At the blasting of the unit spherical charge $i$, the shock pressure of the spherical charge at point A can be expressed as

$$P = K\left(\frac{x + 2id_e}{d_c}\right)^{-\delta} \tag{8}$$

In this case, the shock pressure produced by the entire section of column charges at point A equals the pressure superposition of n unit spherical charges at that point:

$$P_d = \sum_{i=1}^{n} K\left(\frac{x + 2id_e}{d_c}\right)^{-\delta} \tag{9}$$

*3.3. Initial Shock Pressure of Borehole Wall with Middle Air-Decked Charge.* In the middle air-decked charging structure, the length of the air gap is assumed as $l_a$, the charge length at hole bottom as $l_e$, and the length of upper charging section and the lower charging section are $l_1$ and $l_2$, respectively. As shown in Figure 3, a random point A' in the air gap is $x$ ($x \le l_a$) away from the top of the lower charging section. At the blasting of the unit spherical charge $i$, the shock pressure of the spherical charge at point A' can be expressed as

$$P = K\left(\frac{x + 2id_e}{d_c}\right)^{-\delta} \tag{10}$$

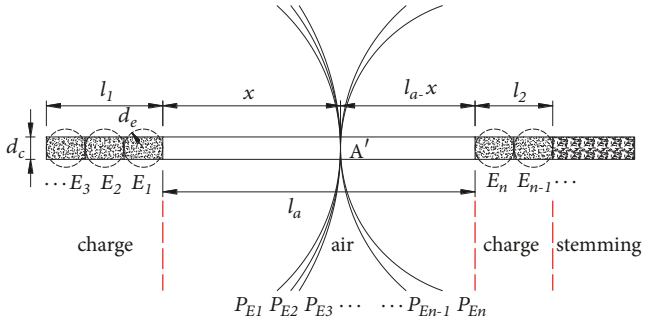


Figure 3: Initial shock pressure of borehole wall with middle air-decked charge.

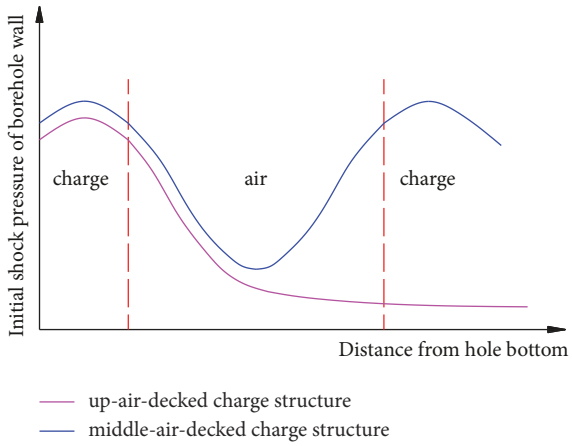


Figure 4: Variation in initial shock pressure of borehole wall.

At the blasting of the unit spherical charge $j$, the shock pressure of the spherical charge at point A' can be expressed as

$$P = K\left(\frac{l_a - x + 2jd_e}{d_c}\right)^{-\delta} \tag{11}$$

In this case, the shock pressure produced by the upper and lower charging sections at point A' equals the pressure superposition of all unit spherical charges at that point:

$$P = \sum_{j=1}^{n_1}\sum_{i=1}^{n_2}\left[K\left(\frac{x + 2id_e}{d_c}\right)^{-\delta} + K\left(\frac{l_a - x + 2jd_e}{d_c}\right)^{-\delta}\right] \tag{12}$$

where $n_1$ and $n_2$ are the number of equivalent unit spherical charges in the upper and lower charging sections, respectively.

The variation curve of the initial shock pressure along the borehole axis of the upper and middle charging structures were derived by (9) and (12) (Figure 4).

## 4. Experiment Verification

*4.1. Pressure Test System.* Based on the principle of resistance strain, the pressure test system applies a dynamic pressure on the specimen, and the resulting deformation of the specimen is recorded by the strain gauges at the measuring points. Then, the deformation-induced resistance change is converted into the change of voltage or current, making it possible to deduce the value of deformation. Here, the pressure at each monitoring point is approximated by Hooke's law, with the aim of reflecting the distribution features of the initial shock pressure of borehole wall along the axial direction.

The test instruments include a Blast-Ultra multichannel shock tester (Chengdu Tytest Co., Ltd.), a KD6009A strain amplifier (Yangzhou Kedong Electronics Co., Ltd.), etc. The strain gauges are attached to prefabricated strain bricks and embedded in a concrete model to receive the explosive signals. The entire test system is illustrated in Figure 5.

*4.2. Preparation of Cement Mortar Models and Strain Bricks.* The 40cm×20cm×50cm (L×W×H) cement mortar model was casted with 42.5# ordinary portland cement and screened fine sands (size: <1mm) at the mix proportion of 1:1:0.5 (cement: sand: water). The model was cured for 28 days at room temperature. The holes (depth: 40cm; blasting burden: 5.5cm) were reversed by a solid fiberglass pipe (OD: 12mm) at 10cm away from the front boundary and the back boundary.

For the upper air-decked charging structure, one 2# Nonel rock detonator was installed at the hole bottom, a 28cm air gap was reserved at the upper part, and the axial decoupling coefficient $K_l$ was set to 5. For the middle air-decked charging structure, one 2# Nonel rock detonator was installed at the hole bottom and the hole collar, respectively, a 21cm air gap was reserved at the middle part, and the axial decoupling coefficient $K_l$ was set to 2.5. In both charging structures, the hole collars were blocked with 5cm long cement plugs (Figure 6).

The strain bricks are 3cm×3cm×40cm (L×W×H) cuboids. These were prepared with the same mix proportion, seeking to prevent the reflection of instantaneous explosion signals and maintain a uniform wave impedance between the model and the bricks [31, 32]. To capture explosion pressure, two strain sticks were arranged in parallel with the holes by a spacing of 2cm. One of them has 8 measuring points and the other has 11 (Figure 6). On each measuring point, two BX120-4AA resistance strain gauges (resistance: 120Ω; sensitivity: 2.08±1%; Yangzhou Kedong Electronics Co., Ltd.) were pasted vertically via half-bridge connection.

Before pasting the strain gauges, the specimen surface was polished with sandpaper at 45° to the axis of the strain brick to remove the sands and gravels. The strain gauges were them pasted with strong glue. The redundant glue must be squeezed out to ensure the good contact between the gauge and the stick.

In the meantime, three standard 5cm×5cm×10cm (L×W×H) specimens were produced and cured for 28 days in the same environment as the models. The physical-mechanical parameters of the models were determined after the curing (Table 2).

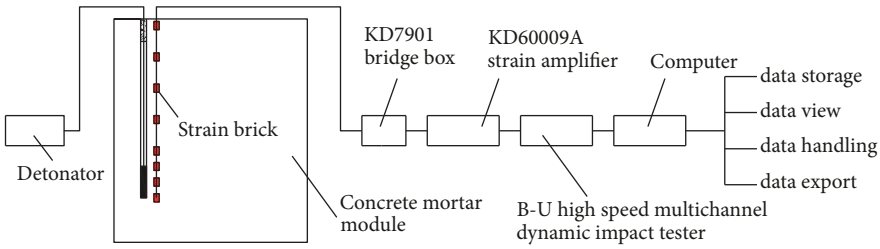


Figure 5: Pressure test system.

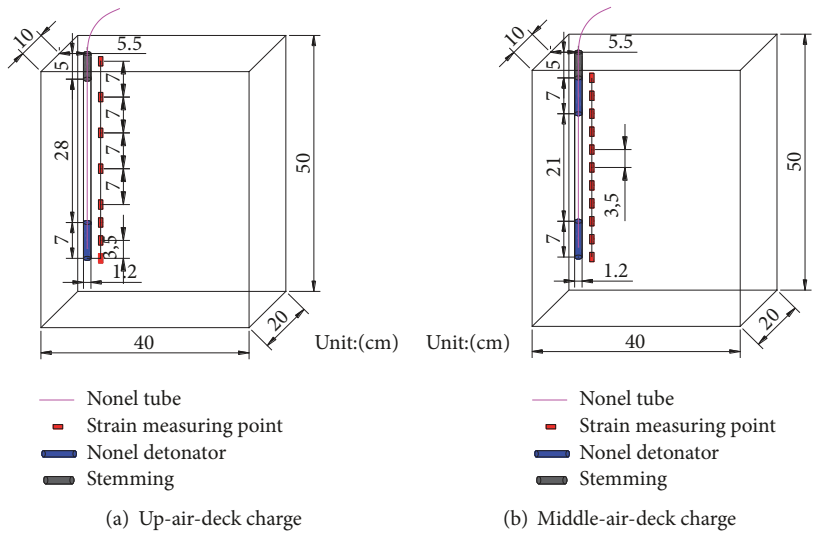


(a) Up-air-deck charge (b) Middle-air-deck charge

Figure 6: The cement mortar model and layout of measuring points.

Table 2: Physical-mechanical parameters of the models.

| Specimen number | Density (kg/m$^3$) | Longitudinal wave velocity (m/s) | Modulus of elasticity (GPa) | Compressive strength(MPa) |
|---|---|---|---|---|
| 1 | 2247.12 | 3115 | 26.44 | 20 |
| 2 | 2153.24 | 3067 | 25.85 | 30 |
| 3 | 2177.00 | 3139 | 24.50 | 20 |
| Average | 2192.45 | 3100 | 25.50 | 23.33 |

*4.3. Experimental Result.* The experimental parameters are as follows: sampling rate=4 each/min, data collection time=10ms, negative delay=1ms, trigger level=5%, gain=100, bridge voltage=2V, and the low-pass frequency=1kHz. The shock pressures of upper and middle air-decked charging structures are recorded in Table 3.

*4.4. Discussion.* Figures 7 and 8 display the test results of the upper and middle air-decked charging structures, respectively. It is clear that the initial shock pressure along the borehole axis obeys the same distribution pattern as that in Figure 4.

(1) For the upper air-decked charging structure, the initial shock pressure of the charging section followed a convex distribution, with the peak value near the charge centre. With the increase in the distance from the charging section, the borehole wall shock pressure in the air gap underwent a sharp decline initially before reaching a relatively constant level. The minimum pressure was observed at the hole collar.

(2) For the middle air-decked charging structure, the pressures at both ends of the charging section obeyed a convex distribution, with the peak value near the charge centre. By contrast, the pressure in the air gap was exhibited as a concave distribution and minimized at the middle of the air column.

(3) In both the upper and middle air-decked charging structures, the initial borehole wall shock pressure increased with the decrease in the distance from the charging section. When that distance was on the rise, the initial pressure experienced a gradual decrease.

Table 3: Experimental results of upper and middle air-decked charging structure.

| Charge structure | Measuring point | Distance from hole bottom (m) | Relative distance from hole bottom | Peak voltage (V) | Peak strain | Peak pressure (MPa) |
|---|---|---|---|---|---|---|
| Up-air-deck charge structure | 1 | 0 | 0 | 2.895 | 14092 | 359.346 |
| | 2 | 0.035 | 2.92 | 3.106 | 15118 | 385.505 |
| | 3 | 0.070 | 5.83 | 2.836 | 14180 | 361.590 |
| | 4 | 0.105 | 8.75 | 2.106 | 10530 | 268.515 |
| | 5 | 0.175 | 14.58 | 1.042 | 5210 | 132.855 |
| | 6 | 0.245 | 20.41 | 0.332 | 1660 | 42.330 |
| | 7 | 0.315 | 26.25 | 0.195 | 975 | 24.863 |
| | 8 | 0.385 | 32.08 | 0.162 | 810 | 20.655 |
| Middle-air-deck charge structure | 1 | 0 | 0 | 3.345 | 16725 | 426.488 |
| | 2 | 0.035 | 2.92 | 3.504 | 17521 | 446.778 |
| | 3 | 0.070 | 5.83 | 3.258 | 16290 | 415.395 |
| | 4 | 0.105 | 8.75 | 2.421 | 12105 | 308.678 |
| | 5 | 0.140 | 11.67 | 1.273 | 6365 | 162.308 |
| | 6 | 0.175 | 14.58 | 1.188 | 5940 | 151.470 |
| | 7 | 0.210 | 17.50 | 1.193 | 5965 | 152.108 |
| | 8 | 0.245 | 20.42 | 2.285 | 11425 | 291.338 |
| | 9 | 0.280 | 23.33 | 3.150 | 15748 | 401.573 |
| | 10 | 0.315 | 26.25 | 3.512 | 17559 | 447.753 |
| | 11 | 0.350 | 29.17 | 3.276 | 16377 | 417.608 |

*Note.* (1) Instead of actual pressure values, the peak pressures obtained by Hooke's law are a rough representation of the distribution features of initial borehole wall shock pressure in the axial direction. (2) The relative distance from hole bottom is the quotient of the distance from hole bottom and the hole diameter.

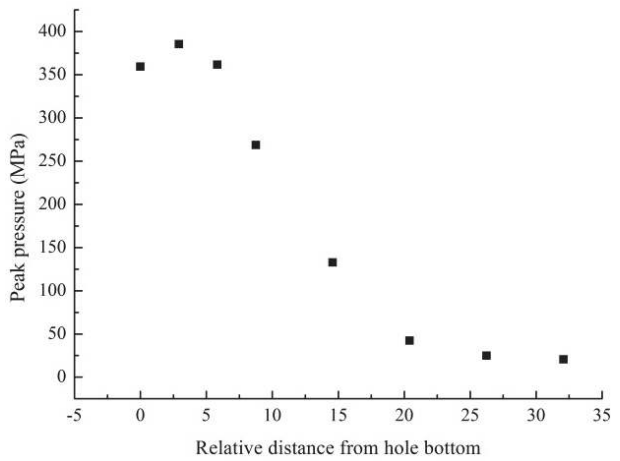


Figure 7: Variation in initial borehole wall pressure with relative distances from hole bottom (upper air-decked charging structure).

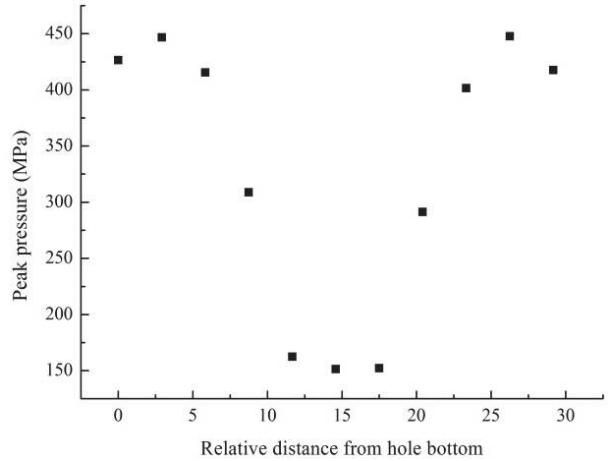


Figure 8: Variation in initial borehole wall pressure with relative distances from hole bottom (middle air-decked charging structure).

The decline rate was fast at the beginning and slow on the later stage. In the end, the borehole wall shock pressure reached a relative stable state.

(4) In the middle air-decked charging structure, the pressure values at major monitoring points in the air gap were close to the minimum value. This feature was particularly prominent when the air space was fairly long. Besides, the initial shock pressure in the upper and lower charge sections obeyed the same distribution of that in the upper air-decked charging structure. The initial shock pressure distribution of the two charge sections could be combined into the superposed impact pressure.

To sum up, the axial distribution curve of the initial borehole wall shock pressure in the two charging structures agrees well with that of the theoretical analysis.

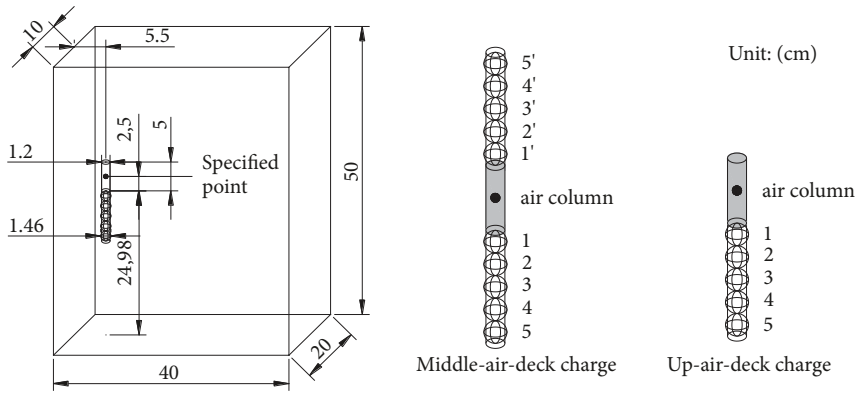


Figure 9: Numerical simulation models.

Table 4: Material model and state equation parameters of the rock.

| Density (kg/m$^3$) | Modulus of elasticity (GPa) | Poisson ratio | Yield stress (MPa) | Tangent modulus (GPa) | Hardening coefficient |
|---|---|---|---|---|---|
| 2350 | 61.0 | 0.31 | 75.0 | 2.0 | 1.0 |

Table 5: Material model and state equation parameters of the explosive.

| Density (kg/m$^3$) | Explosion velocity (m/s) | Detonation pressure (GPa) | $A$ (GPa) | $B$ (GPa) | $R_1$ | $R_2$ | $\omega$ | $E_0$ (GPa) | $V_0$ |
|---|---|---|---|---|---|---|---|---|---|
| 1300 | 4000 | 5.2 | 211.4 | 0.182 | 4.2 | 0.9 | 0.15 | 4.192E6 | 1.0 |

Note: $A$, $B$, $R_1$, $R_2$, and $\omega$ are material model parameters; $R_1$ and $R_2$ are nondimensional parameters; $\omega$ is Grüneisen constant (change rate of pressure relative to internal energy under constant volume); $E_0$ is initial internal energy per unit volume of explosive; $V_0$ is relative volume.

Table 6: Material model and state equation parameters of the air.

| Density (kg/m$^3$) | $C_0$ | $C_1$ | $C_2$ | $C_3$ | $C_4$ | $C_5$ | $C_6$ | $E_0$ (GPa) | $V_0$ |
|---|---|---|---|---|---|---|---|---|---|
| $1.29\times10^{-2}$ | 0 | 0 | 0 | 0 | 0.4 | 0.4 | 0 | 0 | 1.0 |

Note: $C_0 \sim C_6$ are multinomial coefficients of the state equation; $E_0$ is initial internal energy per unit volume of explosive; $V_0$ is relative volume.

## 5. Numerical Simulation

### 5.1. Verification of Theoretical Formula for Initial Shock Pressure

*5.1.1. Numerical Model and Parameters.* Five numerical models were established to verify the accuracy of the theoretical formula derived by Starfield superposition, which calculates the blast-induced initial shock pressure in the air gap. The numerical simulation considers both upper and middle air-decked charging structures, as well as five different charging lengths. In these models, the column charge was 1~4 times longer than equivalent spherical charge. For the middle air-decked charging structure, the lengths of the upper and lower charging sections are both 1~5 times of the diameter of equivalent spherical charge.

As shown in Figure 9, the column charge is 1.2cm in diameter, which puts the diameter of the equivalent spherical charge as 1.46cm according to (1), the length of the reserved air gap is 5cm, and the borehole burden is 5.5 cm. Moreover, the borehole size is Φ1.2 cm×[(1~5)×1.46]cm (the length of column charge)+5 cm (the length of air gap) for the upper air-decked charging structure, and Φ1.2 cm×[2×(1~5) ×1.46]cm (the length of column charge)+5 cm (the length of air gap) for the middle air-decked charging structure. The initiation points were arranged along the charging section at an interval of 1.46cm and designed to initiate simultaneously.

For better accuracy, the rock, explosive, and air were described separately by ∗MAT-PLASTIC-KINEMATIC, ∗MAT-HIGH-EXPLOSIVEBURN, and ∗MAT-NULL models, and the state equations of the explosive and the air were illustrated by ∗EOS-JWL and ∗EOS-LINEAR-POLYNOMAIAL, respectively [33–35]. The parameters of each material model and its state equation are provided in Tables 4–6. Concerning the boundary conditions, the left side and the top of the model were set as free faces, and the other planes as nonreflecting boundaries. Specifically, the explosive and air were processed with Arbitrary-Lagrangian-Eulerian (ALE) algorithm, while the rock was treated by Lagrangian algorithm [36, 37].

Table 7: The charging parameters.

| Axial decoupling coefficients | Hole length (cm) | Stemming length (cm) | Air column length (cm) | Charge length (cm) | | |
|---|---|---|---|---|---|---|
| | | | | Total length (cm) | Upper length (cm) | Lower length (cm) |
| 2.5 | 40 | 5 | 21 | 14 | 4.7 | 9.3 |
| 3.5 | 40 | 5 | 25 | 10 | 3.3 | 6.7 |
| 4.0 | 40 | 5 | 26.25 | 8.75 | 2.9 | 5.85 |
| 5.0 | 40 | 5 | 28 | 7 | 2.3 | 4.7 |
| 6.0 | 40 | 5 | 29.16 | 5.84 | 1.95 | 3.89 |

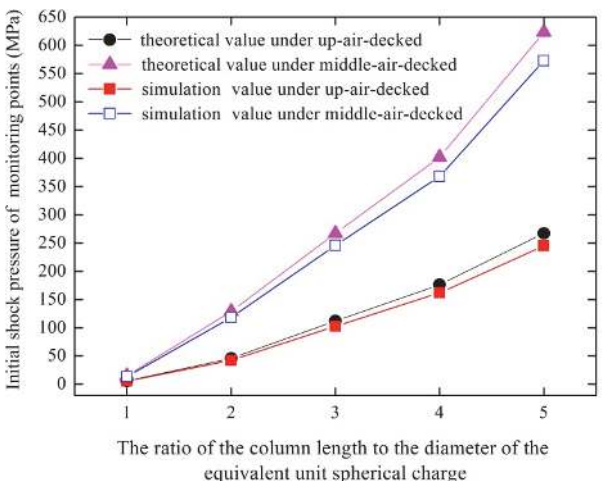


Figure 10: The variation in initial shock pressure with column lengths at specified points.

*5.1.2. Result Analysis.* The intersection points between the borehole wall and the axial cross-section of air column, which is far away from free faces, were selected to monitor the initial shock pressure of borehole wall. Through simulation, two sets of initial shock pressure values were obtained from the monitoring points for upper and middle air-decked charging structures. Meanwhile, the shock pressures at the specified points were acquired through theoretical analysis.

Figure 10 compares the theoretical and simulated values of initial shock pressures at the specified points under the two charging conditions. It can be seen that the simulated pressures deviated from the results of (9) by 8.82% and those of (12) by 8.96%. Since neither of the deviations surpassed 10%, the simulated results agree well with the conclusion of theoretical analysis, an evidence to the reliability of the theoretical formula derived from the Starfield superposition under both upper and middle air-decked charging conditions.

Furthermore, the theoretical and simulated initial shock pressure at specified points of the air gap increased with the charging length, according to the variation in initial shock pressure with column lengths at specified points. The trend echoes with the classical blasting theory.

### 5.2. Verification on Axial Distribution Pattern of Initial Borehole Shock Pressure

*5.2.1. Numerical Model and Parameters.* The author established the numerical models by ANSYS/LS-DYNA, using the same dimension, borehole size, and borehole pattern with the test model (Figure 11). For the upper air-decked charging structure, five models were created with different axial decoupling coefficients: $K_l$=2.5, $K_l$ =3.5, $K_l$ =4, $K_l$=5.0, and $K_l$ =6.0. Among them, $K_l$ =5.0 corresponds to the charging structure of the test model. In this charging structure, the overall charging length equals the length of the lower charging section.

For the middle air-decked charging structure, five models were created with different axial decoupling coefficients: $K_l$=2.5, $K_l$ =3.5, $K_l$ =4, $K_l$=5.0, and $K_l$ =6.0. Among them, $K_l$ =2.5 corresponds to the charging structure of the test model. The charging parameters of these models are shown in Table 7. In this charging structure, the overall charging length equals the sum of the length of the upper and lower charging section.

The material models of the rock, explosive, and air and the relevant state equations (Tables 4–6) are the same with those in the verification of theoretical formula for the initial borehole wall shock pressure. The stemming material is described by the ∗MAT-SOIL-AND-FOAM model, and its parameters are shown in Table 8.

*5.2.2. Results and Discussion.* To capture the initial borehole wall shock pressure, row elements were selected from borehole wall as pressure monitoring points along the axial direction from hole bottom to hole collar. Figures 12 and 13 depict the distribution curves of the initial shock pressure along the borehole axis under different decoupling coefficients, respectively.

As shown in Figures 12-13, the simulated pressure distributions of the two charging structures are similar to those obtained by theoretical analysis. In particular, the curves at $K_l$ = 5.0 of the upper air-decked charging structure and $K_l$ =2.5 of the middle air-decked charging are consistent with the theoretical results and the experimental findings. Suffice it to say that the simulation demonstrates the reliability of theoretical analysis and physical experiments.

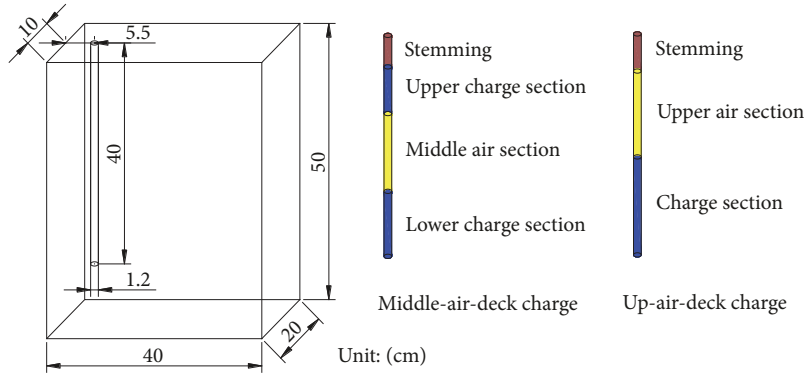


Figure 11: Numerical simulation models.

Table 8: Parameters of the stemming material.

| Density (kg/m$^3$) | Shear modulus (GPa) | Bulk modulus(GPa) | $A_0$ | $A_1$ | $A_2$ | *PC* | *EPS1* | *EPS2* |
|---|---|---|---|---|---|---|---|---|
| 1800 | 1.60E-2 | 1.328 | 0.0033 | 1.31E-7 | 0.1232 | 0.0 | 0.0 | 0.05 |
| *EPS3* | *EPS4* | *EPS5* | *EPS6* | *EPS7* | *EPS8* | *EPS9* | *EPS10* | $P_1$(GPa) |
| 0.09 | 0.11 | 0.15 | 0.19 | 0.21 | 0.221 | 0.25 | 0.30 | 0.0 |
| $P_2$ (GPa) | $P_3$ (GPa) | $P_4$ (GPa) | $P_5$ (GPa) | $P_6$ (GPa) | $P_7$ (GPa) | $P_8$ (GPa) | $P_9$ (GPa) | $P_{10}$ (GPa) |
| 3.42 | 4.53 | 6.76 | 12.70 | 20.80 | 27.10 | 39.20 | 56.60 | 123.0 |

Note: $A_0$, $A_1$, and $A_2$ are constants of yield function; *PC* is truncation pressure of tensile failure; *EPS1*~ *EPS10* are characteristic bulk strains; $P_1 \sim P_{10}$ are pressures corresponding to characteristic bulk strains.

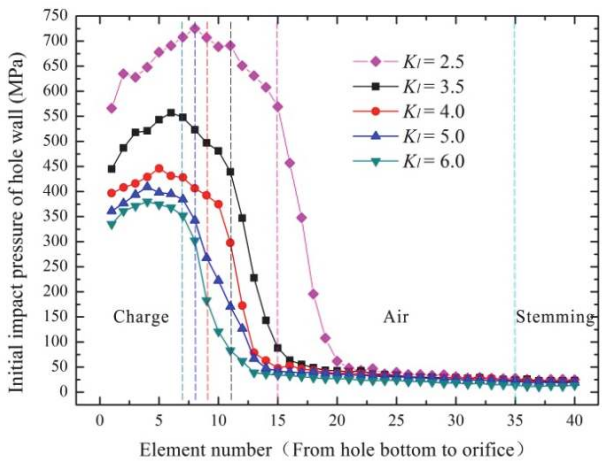


Figure 12: Initial shock pressure of borehole wall with upper air-decked charging structure.

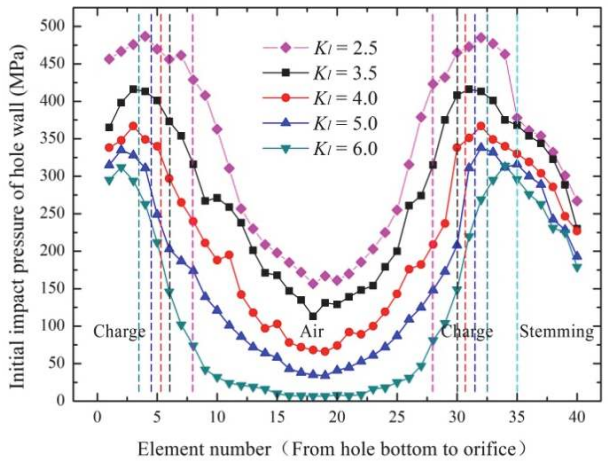


Figure 13: Initial shock pressure of borehole wall with middle air-decked charging structure.

## 6. Case Study and Comparative Model Test of Blasting Vibration

*6.1. Case Study.* The borehole length in a single blasting row is relatively long in Grade III surrounding rock of Banjie tunnel. To ensure the effect of smooth blasting, the peripheral hole was designed with air-decked charging structure. In the middle air-decked charging structure, the initial borehole wall shock pressure obeyed a wavy distribution (peak value> valley value>0). The peak and valley values, respectively, correspond to the charging section and the air gap. To achieve a consistent impedance of the explosive and rock, it is necessary to appropriate the length of the air column [38].

In Banjie tunnel, the compressive strength and tensile strength of Grade III surrounding rock are 75MPa and 5.6MPa, respectively (Table 1). According to the simulated distribution of initial borehole wall shock pressure in middle air-decked charging structure (Figure 13), the initial shock pressures in the air gap were all higher than the tensile strength of the rock when the axial decoupling coefficient

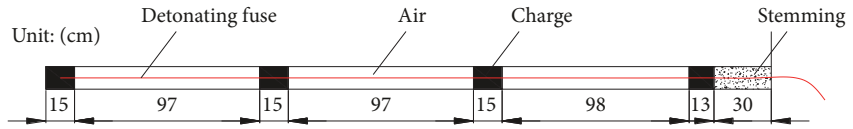


Figure 14: Optimized charging structure of peripheral hole in Grade III surrounding rock.

Table 9: Comparison of blasting vibration vector synthesis velocity.

| Distance from explosive source(cm) | 10 | 20 | 40 | 80 |
|---|---|---|---|---|
| Vector synthesis velocity of blasting vibration in model I(cm/s) | 20.1759 | 9.3194 | 6.0529 | 3.4562 |
| Vector synthesis velocity of blasting vibration in model II(cm/s) | 17.3309 | 8.0813 | 5.1540 | 2.9053 |
| Relative decreasing amplitude ratio (%) | 14.10 | 15.32 | 14.85 | 15.94 |

varied in the range of $K_l$ =2.5~6. This means blasting cracks formed among the adjacent peripheral holes. However, the shock pressures at major monitoring points in the air gap were above the compressive strength of the rock, when $K_l$=2.5, $K_l$ =3.5, $K_l$ =4.0, and $K_l$ =5.0. The result shows that the rock was crushed but not sufficient to achieve a good smooth blasting effect.

In contrast, when $K_l$ =6.0, the pressures at most monitoring points in the air gap were close to the valley value, except the charging section and a small portion of the air gap, and were below the compressive strength of the rock. In this case, the surrounding rock remained integrated after the blast and kept a half-hole profile, revealing enhanced smooth blasting effect. Therefore, the axial decoupling coefficients of the peripheral hole were designed as $K_l$ =6.0 in Grade III surrounding rock of Banjie tunnel. In light of the field conditions, four-stage charges and three air-gaps were adopted for tunnelling. The optimized charging structure of peripheral hole in Grade III rock is given in Figure 14.

In Figure 14, the hole profile is clearly visible after blasting, and over 90% of half-holes are reserved. According to the blasting effect in Figure 15, there is barely any overbreak or underbreak after excavation, and the surrounding rock remained stable for a long time.

*6.2. Comparative Model Test of Blasting Vibration.* In tunnel blasting, the vibration, a key impact factor of rock stability, is the combined effect of the blasting of cutting holes, auxiliary holes, and peripheral holes. However, it is difficult to accurately extract the variation induced by the blasting of peripheral holes in field monitoring. To compare the blasting vibration of continuous bottom charging with air-decked charging structure, two 100cm×20cm×60cm (L×W×H) cement mortar models, denoted as model I and model II, respectively, were prepared for blasting experiment.

The mix proportion, curing environment, and curing time were exactly the same as the cement mortar models

Figure 15: Optimized smooth blasting effect of Grade III surrounding rock.

of Section 4.2. One borehole (depth: 40cm; blasting burden: 5.5cm) was reversed at 10cm away from the front boundary and the back boundary. With the same explosive payload, Models I and II, respectively, adopt continuous bottom charging and air-decked charging. The blasting was monitored by sensors placed at 10cm, 20cm, 40cm, and 80cm away from borehole. Figure 16 illustrates the cement mortar models and the layout of vibration measuring points.

The monitoring results are shown in Table 9, and the typical waveforms of vibration vector synthesis velocities are given in Figure 17. As can be seen in Table 9, the vibration velocity of model II was much lower than that of model 1 at the same distance from borehole, revealing the good damping effect of air-deck blasting. Compared with continuous bottom charging, the air-decked blasting structure had a 15.05% lower average amplitude under the same explosive payload. Thus, the air-decked blasting structure can reduce the integer blasting vibration velocity during the tunnelling in Grade III surrounding rock of Banjie tunnel and, in turn, assure the stability of the surrounding rock.

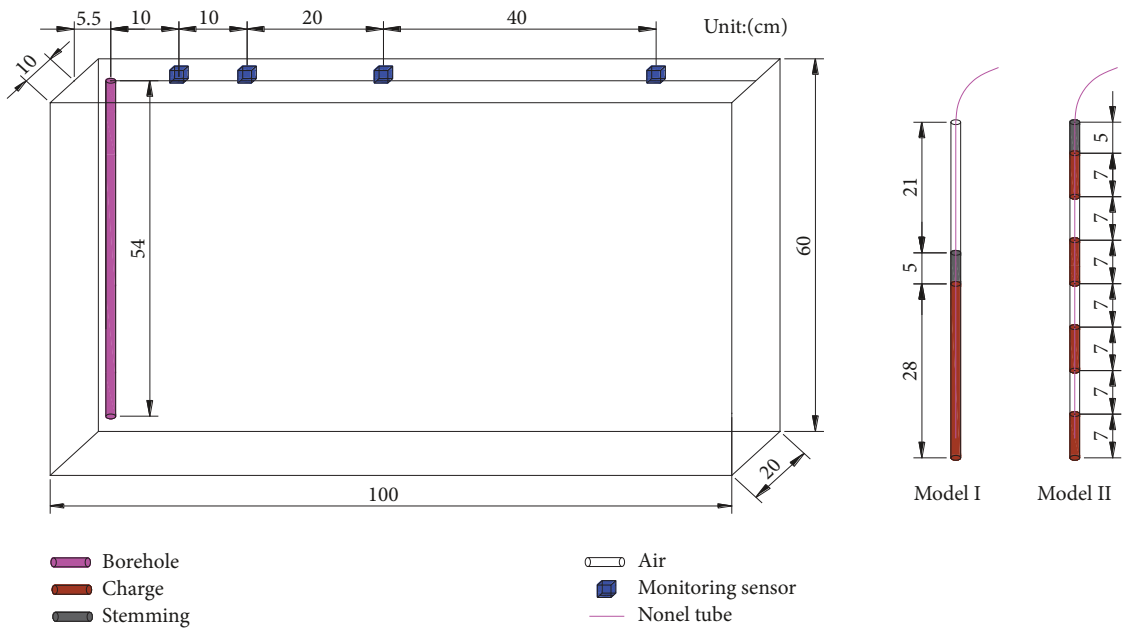


Figure 16: The cement mortar models and layout of vibration measuring points.

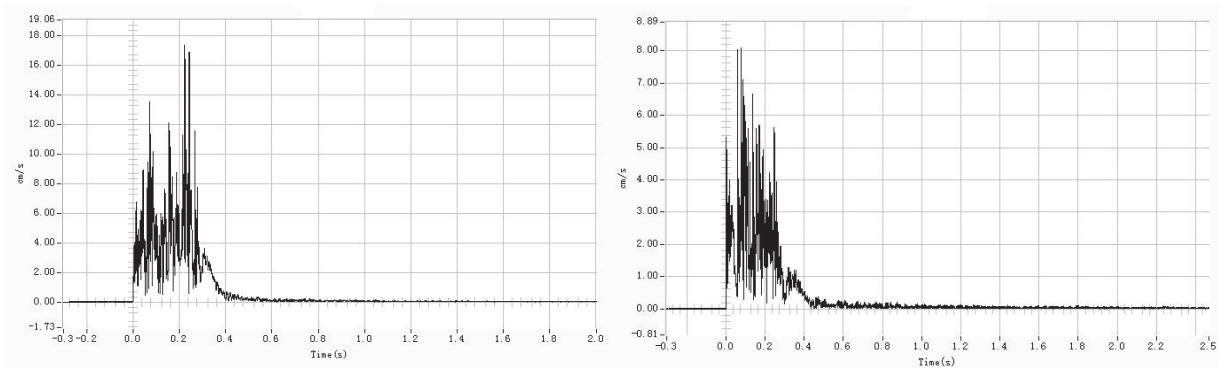


Figure 17: Typical waveforms of blasting vibration vector synthesis velocity.

## 7. Conclusions

(1) Based on Starfield superposition, the theoretical solutions of the initial pressure on borehole wall were obtained for upper and middle decked charged structures. Through field monitoring and numerical simulation, it is learned that the initial borehole wall pressure was unevenly distributed at long air columns.

(2) For the upper air-decked charging structure, the initial shock pressure of the charging section followed a convex distribution, with the peak value near the charge centre. With the increase in the distance from the charging section, the borehole wall shock pressure in the air gap underwent a sharp decline initially before reaching a relatively constant level. The minimum pressure was observed at the hole collar. For the middle air-decked charging structure, the pressures at both ends of the charging section obeyed a convex distribution, with the peak value near the charge centre.

(3) The deviations between simulated and theoretical pressures are smaller than 10%, indicating the reliability of the theoretical formula derived by Starfield superposition. It is concluded that this formula works well in computing the blasting-induced initial shock pressure in the air gap under both upper and middle air-decked charging conditions.

(4) Compared with the continuous bottom charging, the air-decked charging is suitable to the actual conditions thanks to the distribution features of initial borehole wall shock pressure. The application of the structure in Grade III surrounding rock of Banjie tunnel led to an expected smooth blasting effect.

(5) The research findings provide valuable references to the theoretical and experimental calculation of air column length and other key parameters of air-deck

blasting and shed new light on the charging structure determination of smooth blasting and blasting vibration control for the excavation of large-section, deep mining roadways.

## Conflicts of Interest

The authors declare that there are no conflicts of interest regarding the publication of this paper.

## Acknowledgments

This research work was supported by the National Natural Science Foundation of China under Grants 51679093 and 51374112.

## References

[1] J.-H. Chen, J.-S. Zhang, and X.-P. Li, "Study of presplitting blasting parameters and its application based on rock blasting-induced damage theory," *Rock and Soil Mechanics*, vol. 37, no. 5, pp. 1441–1450, 2016.

[2] E. Kabwe, "Improving collar zone fragmentation by top air-deck blasting technique," *Geotechnical and Geological Engineering*, vol. 35, no. 1, pp. 157–167, 2017.

[3] J. C. Jhanwar and J. L. Jethwa, "The use of air decks in production blasting in an open pit coal mine," *Geotechnical and Geological Engineering*, vol. 18, no. 4, pp. 269–287, 2000.

[4] W. L. Fourney, D. B. Barker, and D. C. Holloway, "Model studies of explosive well stimulation techniques," *International Journal of Rock Mechanics and Mining Sciences and Geomechanics Abstracts*, vol. 18, no. 2, pp. 113–127, 1981.

[5] G. L. Yang, R. S. Yang, C. Huo, and Y. L. Che, "Numerical simulation of air-deck slotted charge blasting," *Advanced Materials Research*, vol. 143-144, pp. 787–791, 2011.

[6] M. R. Saharan, M. Sazid, and T. N. Singh, "Explosive Energy Utilization Enhancement with Air-Decking and Stemming Plug, "SPARSH"," in *Proceedings of the ISRM European Rock Mechanics Symposium, EUROCK 2017*, vol. 191, pp. 1211–1217, Czech, June 2017.

[7] D. H. Park and S. W. Jeon, "Reduction of blast-induced vibration in the direction of tunneling using an air-deck at the bottom of a blasthole," *International Journal of Rock Mechanics and Mining Sciences*, vol. 47, no. 5, pp. 752–761, 2010.

[8] S. K. Roy, R. R. Singh, R. Kumar, and U. K. Dey, "Studies into possible use of air decking in solid blasting in Indian underground coal mines," *Transactions of the Institutions of Mining and Metallurgy, Section A: Mining Technology*, vol. 117, no. 2, pp. 83–92, 2008.

[9] S. Esen, I. Onederra, and H. A. Bilgin, "Modelling the size of the crushed zone around a blasthole," *International Journal of Rock Mechanics and Mining Sciences*, vol. 40, no. 4, pp. 485–495, 2003.

[10] C. Cunningham, "Concepts of blast hole pressure applied to blast design," *Fragblast*, vol. 10, no. 1-2, pp. 33–45, 2006.

[11] O. Francis, "Measurements and prsesdictions of borehole pressure variations in model blasting system," in *Proceedings of the 1st International Symposium on Rock Fragmentation by Blasting*, pp. 7–20, Lulea, Sweden, 1983.

[12] P. J. Hommert, J. S. Kuszmaul, and R. L. Parrish, "Computational and experimental studies of the role of stemming in cratering," in *Proceedings of the 2nd International Symposium on Rock Fragmentation by Blasting*, pp. 550–562, Colorado, Keystone, 1987.

[13] G. Swoboda, "The numerical modelling of blast loading," in *Proceedings of the International Symposium on Application of Computer Methods in Rock Mechnics and Engineering*, Xian, China, 1993.

[14] L. Liu and P. D. Katsabanis, "A theoretical approach to the stress waves around a borehole and their effect on rock crushing," in *Proceedings of the 4th International Symposium on Rock Fragmentation by Blasting*, pp. 10–13, Vienna, Austria, 1993.

[15] O. Yilmaz and T. Unlu, "Three dimensional numerical rock damage analysis under blasting load," *Tunnelling and Underground Space Technology Incorporating Trenchless Technology Research*, vol. 38, no. 9, pp. 266–278, 2013.

[16] S. Nie and M. Olsson, "Study of fracture mechanism by measuring pressure history in blastholes and crack lengths in rock," in *Proceedings of the 27th Annual Conf. Explosives and Blasting Technique*, Orlando, Florida, USA, 2000.

[17] A. Persson, R. Holmberg, and J. Lee, "Rock blasting and explosives engineering," *International Journal of Rock Mechanics and Mining Sciences and Geomechanics Abstracts*, vol. 32, no. 6, p. 278A, 1995.

[18] N. Jiang, C. B. Zhou, X. D. Luo, and S. Lu, "Damage characteristics of surrounding rock subjected to VCR mining blasting shock," *Shock and Vibration*, vol. 2015, Article ID 373021, 8 pages, 2015.

[19] L. Wu, Y. Zhou, and Z. Guo, "The rock failure mechanism of air-decked blasting in hole bottom," *Applied Mechanics and Materials*, vol. 201-202, pp. 375–378, 2012.

[20] D. J. Xiao, B. Li, C. J. Pu, and H. Q. Zhou, "Model test and numerical simulation for directional pressure relief blasting," *Advanced Materials Research*, vol. 779, pp. 848–856, 2013.

[21] Q. Ma, P. Yuan, J. Zhang, R. Ma, and B. Han, "Blast-induced damage on millisecond blasting model test with multicircle vertical blastholes," *Shock and Vibration*, vol. 2015, Article ID 504043, 6 pages, 2015.

[22] H. Zhao, X. P. Li, and Q. Dong, "The research of similar material and dosage in blasting model test," *Applied Mechanics and Materials*, vol. 724, pp. 152–155, 2015.

[23] G.-L. Yang, R.-S. Yang, and L.-L. Jiang, "Pressure distribution along borehole with axial air-deck charge blasting," *Explosion and Shock Waves*, vol. 32, no. 6, pp. 653–657, 2012.

[24] W. M. Ling, "Experimental research on explosion pressure on the wall of a borehole in rock," *Mining and Metallurgy*, vol. 13, no. 4, pp. 13–16, 2004.

[25] Z. F. Ni and Y. M. Li, "Theoretical calculation and regression on initial shock wave pressure of borehole in rock blasting," *Chinese Journal of Rock Mechanics and Engineering*, vol. A1, pp. 511–514, 1996.

[26] X. H. Jin, Y. Sha, and R. Wang, "Analysis on breakage from blasting crater of column charge," *Water Resources and Hydropower Engineering*, vol. 41, no. 11, pp. 48–51, 2010.

[27] W. L. Wang, *Drilling and Blasting*, China Coal Industry Publishing House, Beijing, China, 1984.

[28] G. Harries, "The modeling of long cylindrical charge of explosive," in *Proceedings of the 1st International Symposium on Rock Fragmentation by Blasting*, pp. 419–431, Lulea, Sweden, 1983.

[29] W. B. Lu, *The Propagation of Stress Wave and Its Effects in Rock Blasting*, Wuhan University of Hydraulic and Electric Engineering, Wuhan, China, 1994.

[30] J. Henrych and G. R. Abrahamson, "The dynamics of explosion and its use," *Journal of Applied Mechanics*, vol. 47, no. 1, p. 218, 1980.

[31] Q. Zong, *Tunneling Blasting Parameters Model Experiment Study on Vertical Well Freezing Soil*, University of Science and Technology China, Hefei, China, 2004.

[32] J. J. Ma, Z. Z. Xiong, W. D. Duan, D. W. Zhong, and L. J. Cai, "Theoretical testing study factors affecting parallel hole cut blasting," *Journal of University of science and Technology (Natural science edition)*, vol. 24, no. 2, pp. 170–174, 2001.

[33] Y. F. Chen and G. X. Yi, "Dynamic response analysis of the reinforced concrete column under the effect of explosive impact load," *Advanced Materials Research*, vol. 681, pp. 99–104, 2013.

[34] I. A. Balagansky and A. A. Stepanov, "Numerical simulation of Composition B high explosive charge desensitization in gap test assembly after loading by precursor wave," *Shock Waves*, vol. 26, no. 2, pp. 109–115, 2016.

[35] P. Yan, W. Zhou, W. Lu, M. Chen, and C. Zhou, "Simulation of bench blasting considering fragmentation size distribution," *International Journal of Impact Engineering*, vol. 90, pp. 132–145, 2016.

[36] Y. Han and H. Liu, "Finite element simulation of medium-range blast loading using LS-DYNA," *Shock and Vibration*, vol. 2015, Article ID 631493, 9 pages, 2015.

[37] D. Su, Y. Kang, D. Li, X. Wang, and F. Yan, "Analysis and numerical simulation on the reduction effect of stress waves caused by water jet slotting near blasting source," *Shock and Vibration*, vol. 2016, Article ID 5640947, 18 pages, 2016.

[38] W.-B. Gu, Z.-X. Wang, J.-H. Chen, J.-Q. Liu, and M. Lu, "Experimental and theoretical study on influence of different charging structures on blasting vibration energy," *Shock and Vibration*, vol. 2015, Article ID 248739, 11 pages, 2015.